Transport Simulations of a Density Limit in Radiation-Dominated Tokamak Discharges - Profile Effects

D. P. Stotler

Plasma Physics Laboratory

Princeton University

Princeton, New Jersey 08543

ABSTRACT

The density limit observed in tokamak experiments is thought to be due to a radiative collapse of the current channel. A transport code coupled with an MHD equilibrium routine is used to determine the detailed, self-consistent evolution of the plasma profiles in tokamak discharges with radiated power close to or equalling the input power. The present work is confined to ohmic discharges in steady state. It is found that the shape of the density profile can have a significant impact on the variation of the maximum electron density with plasma current. Analytic calculations confirm this result.

MASTER

I. Introduction

The limit on density observed in present tokamak experiments is not of much interest except as a parameter space boundary that is to be avoided. However, in a burning plasma it represents a limit to the amount of fusion power that can be produced; that is, it restricts the value of $n\tau_E$ (n is the plasma density, τ_E is the energy confinement time) that can be achieved. In fact, transport simulations of two recent reactor designs[1] and the Compact Ignition Tokamak[2,3] (CIT) do not predict ignition with an L-mode[4] scaling for τ_E when the density is required to remain below that predicted by present expressions for the density limit. Several formulas for the density limit are now in use, and most match recent data very well. However, when extrapolated to high fields and significantly noncircular cross sections, their predictions vary considerably. In an attempt to reduce the uncertainty in the density limit scaling law, we will use the 1-1/2-D BALDUR[5,6] transport code to simulate high density tokamak discharges. Hopefully, this will lead to a model of the density limit with a predictive capability. If the procedure is successful, the resulting model could be used to optimize the design of future ignition devices. In this paper we will describe the first step in the development of such a simulation model and will show results for ohmic discharges. Later work will include detailed comparisons with experiments.

The first scaling law for the maximum density in tokamaks was proposed by Murakami et al.[7] They noted that $\overline{n_{e,max}} \propto B_T/R$, where $\overline{n_e}$ is the line-averaged electron density, B_T is the toroidal magnetic field, and R is the plasma major radius. This scaling was later refined to include a dependence on the plasma current through the safety factor, q; namely,[8] $\overline{n_{e,max}} \propto B_T/Rq$. A density limit expressed in this form is often referred to as the Hugill limit. The Murakami limit is then the maximum density for all values of the plasma current.

It is not clear how to extend the scaling law for the Hugill limit to include tokamaks having elongated cross sections due to the wide variety of analytic expressions for q and its cylindrical equivalent, q_{cyl}. Greenwald has recently made an attempt to consolidate the data from machines of various shapes and sizes.[9,10] He concluded that a tokamak with a high power density, low impurity level, and efficient central fuelling is limited to a density $\overline{n_{e,G}} = \kappa J \times 10^{20} m^{-3}$, where κ is the plasma elongation and J is the average plasma

current density (in MA/m^2). Compared to present Hugill-type scalings, this expression tends to be more favorable for highly elongated reactor designs.

Unfortunately, the range of κ covered in the present data base is not sufficient to rule out clearly the Hugill-type scalings. For example, the maximum density observed in the Joint European Torus (JET)[11] is $\overline{n}_{e,max} = 2B_T/Rq_e$, where $q_e = 5a^2\kappa B_T/RI_p$ is referred to as the engineering safety factor. Note that we express B_T in T, a (the plasma minor radius) and R in m, and I_p (the plasma current) in MA. Given the uncertainties in the experimental measurements and the limitation to $\kappa < 1.7$ in the JET device, it is difficult to discern between this and the Greenwald expression. Yet, the values they predict differ significantly at elongations of $\kappa \geq 2$, typical of reactor designs. The more theoretical approach of transport simulation could provide one means of bridging this gap in the data base.

Most of the explanations proposed to date for the density limit rely upon impurity radiation-induced profile changes as the primary cause of the disruption.[12-17] However, one of the conclusions drawn by Greenwald is that the maximum density obtainable for a given current is determined not by radiation, but by a deterioration of the particle confinement in the plasma core. Due to the lack of detailed models for this process, transport codes can do little to clarify the situation except to provide a means for carrying out the arduous task of preparing complete simulations of particular discharges. We can, however, examine with relative ease many of the consequences of impurity radiation. Therefore, we confine our attention in the present work to discharges dominated by impurity line radiation.

The model used for this radiation is of great importance. Most of the theoretical work carried out so far has employed the coronal equilibrium model[18] due to its relative simplicity. However, the model is known to yield radiated power levels that are far below those found in actual experiments.[19] On the other hand, by using an empirically determined scaling for the radiation in JET, Campbell et al.[20] were able to derive a reasonable expression for the density limit simply by balancing the radiated power and the total input power. There are limitations on the parameters for which this expression is applicable; hence, there is a need for more theoretical input. Computer codes capable of accurately modelling the radiation in systems deviating from coronal equilibrium are presently being used in the analysis of tokamak data.[21] Hopefully, these same techniques can be applied to studies of the density

3

limit.

With a 1-1/2-D transport code, we can investigate self-consistent, time-dependent profile effects. We have complete freedom in the specification of transport models and plasma compositions. Plasma fuelling by gas puffing and pellet injection can both be modelled. In addition to ohmic heating, auxiliary input power from neutral beam injection or other sources can be included. By coupling the transport code to an equilibrium code, we can investigate MHD effects in detail. For example, sawtooth oscillations and tearing modes (currently being installed in the BALDUR code[22]) will have a significant impact on the discharges we investigate.

The present work is limited to steady-state simulations of ohmic discharges; a TFTR geometry is used.[23] In particular, we focus on density profile effects. The most important difference between flat and peaked density profiles is that, for a given volume-averaged density, a flat profile has a higher density near the edge. It is in this low temperature edge region that the impurity line radiation (proportional to the local product of the electron density and the impurity density) peaks. The higher density in the flat profile case leads to a greater contribution to the overall radiated power. Hence, flat profile cases are restricted to lower average densities than peaked profile discharges with the same input power.

What is more surprising is that in simulations with centrally peaked density profiles (edge density much less than central density) there is a significant variation in the critical Murakami parameter with q_{cyl}, as observed experimentally (i.e., the Hugill limit). On the other hand, with flat profiles (edge density slightly less than central density), the critical Murakami parameter is almost independent of q_{cyl}. We show analytically that these results are a consequence of the effect changing q_{cyl} has on the sawtooth mixing radius, (in our model) the electron temperature profile, and safety factor profile.

In Sec. II, we specify the simulation model we will be using. We give our numerical results in Sec. III. The analytic calculations will be described in Sec. IV. Finally, a discussion and summary is presented in Sec. V.

II.   Simulation Model

We now describe briefly our transport code and discuss the models and assumptions used in the simulations. We employ the 1-1/2-D BALDUR

4

transport code; details on it have been given elsewhere.[5,6] It integrates in time a set of flux-surface-averaged transport equations on a radial grid of surfaces of constant toroidal flux. Their shape is provided by a set of moments equilibrium routines that are interfaced with the transport code. The transport equations solved describe the diffusion of density, energy, and magnetic field:

$$\left.\frac{\partial}{\partial t}\right|_{\xi} (nV') = -\frac{\partial}{\partial \xi}(V'\langle \boldsymbol{\Gamma}_\rho \cdot \boldsymbol{\nabla}\xi\rangle - nV''\dot{\rho}/\rho') + V'\langle S\rangle, \tag{1}$$

$$\frac{3}{2}\left.\frac{\partial}{\partial t}\right|_{\xi} (nTV') = -\frac{\partial}{\partial \xi}\left(V'\langle \boldsymbol{q}_\rho \cdot \boldsymbol{\nabla}\xi\rangle - \frac{3}{2}\frac{nTV''\dot{\rho}}{\rho'}\right)$$
$$- V'\langle Q\rangle - nT\left[\dot{V}' - (\dot{\rho}V''/\rho')'\right], \tag{2}$$

$$\left.\frac{\partial}{\partial t}\right|_{\xi} (B_p\rho') = \frac{\partial}{\partial \xi}\left\{\frac{\eta}{I\langle 1/R^2\rangle}\left[\frac{I^2}{\mu_0 V'}\frac{\partial}{\partial \xi}\left(\frac{V'\rho'B_p}{I}\left\langle\frac{\boldsymbol{\nabla}\xi|^2}{R^2}\right\rangle\right)\right.\right.$$
$$\left.\left. - \frac{\langle \boldsymbol{J}_{beam} \cdot \boldsymbol{B}\rangle}{R_{0REF}} - \frac{\langle \boldsymbol{J}_{boot} \cdot \boldsymbol{B}\rangle}{R_{0REF}}\right] - \dot{\rho}B_p\right\}. \tag{3}$$

There are separate equations for the density, $n(\xi, t)$, of each ionic species. The electron density is computed from quasi-neutrality. Separate energy equations are solved for ions and electrons; the temperatures, $T(\xi, t)$, of all ionic species are taken to be equal. The quantity appearing in Eq. (3) is actually a normalized poloidal flux gradient:

$$B_p \equiv \frac{\partial \psi_{pol}/\partial \rho}{2\pi R_{0REF}}. \tag{4}$$

In the limit of a circular cylinder geometry, this B_p reduces to the actual poloidal magnetic field. Note that ρ is a flux-surface label defined by $\rho \equiv (\psi_{tor}/\pi B_{0REF})^{1/2}$; B_{0REF} and R_{0REF} are a fixed reference magnetic field and major radius, respectively. The equations have been transformed into a coordinate system with arbitrary flux surface label ξ. The toroidal (poloidal) fluxes are denoted by ψ_{tor} (ψ_{pol}). The volume inside flux surface ξ is $V(\xi, t)$; $V' = \partial V/\partial \xi$. An overdot indicates a derivative with respect to time . The particle and heat fluxes are designated as $\boldsymbol{\Gamma}_\rho$ and $\boldsymbol{q}_\rho$. The subscript ρ signifies that they are defined relative to surfaces of constant toroidal flux. Volume

5

sources of particles (energy) are contained in S (Q). Finally, in the magnetic diffusion equation, Eq. (3). R is the major radius. η is the plasma resistivity. and $I(\xi) = RB_T$, where B_T is the toroidal magnetic field. We show for completeness contributions from beam-driven current (J_{beam}) and bootstrap current (J_{boot}), although we do not make use of either in these simulations. In all cases. the angle brackets denote a flux-surface average.

We will keep the expressions for the fluxes relatively simple in order to focus on the effects of radiation in the power balance. The expression we use for the heat flux is

$$\langle q_\rho \cdot \nabla \xi \rangle_j = \left(-\chi_j \frac{\partial}{\partial \xi} \left\langle \frac{3}{2} n_j T_j \right\rangle \langle |\nabla \xi| \rangle + \frac{3}{2} T_j \langle \Gamma_\rho \cdot \nabla \xi \rangle_j \right) \frac{\langle |\nabla \xi|^2 \rangle}{\langle |\nabla \xi| \rangle}, \qquad (5)$$

where the subscript j denotes electron or ion thermal flux. In this particular version of BALDUR, the flux-surface label, ξ, is taken to be the square root of the normalized toroidal flux, $\xi = (\psi_{tor}/\psi_{tor,a})^{1/2}$, where $\psi_{tor,a}$ is the toroidal flux at the plasma boundary.

The thermal diffusivities are based upon the INTOR model.[24] They should give rise to a neo-Alcator type scaling for the energy confinement time. as is appropriate for an ohmic discharge. One could argue that this is not suitable at the highest densities where a saturation of the energy confinement time with density is usually observed.[25] In the interest of simplicity, however. we use the following model for all of the simulations discussed here. We set

$$\chi_e = 2.6/n_{e,19}(\xi) + \chi_e^{NC}, \qquad (6)$$

and

$$\chi_i = 1.3/n_{e,19}(\xi) + \chi_i^{CH}. \qquad (7)$$

The units on both are m^2/sec; $n_{e,19}(\xi)$ is the local electron density in units of $10^{19}\ m^{-3}$. The neoclassical contribution computed by Chang and Hinton[26] is included as χ_i^{CH}. The neoclassical electron thermal diffusivity χ_e^{NC} is also included; see Ref. 5 for the detailed expression. The overall constants in Eqs. (6) and (7) have been chosen to yield reasonable central temperatures in a steady-state, ohmic TFTR discharge (~ 2.5 keV, see for example Ref. 27).

The particle flux of ionic species j is written as

$$\langle \Gamma_\rho \cdot \nabla \xi \rangle_j = \left(-D_j \frac{\partial n_j}{\partial \xi} \langle |\nabla \xi| \rangle + n_j v_j - \Gamma_j^{neo} \right) \frac{\langle |\nabla \xi|^2 \rangle}{\langle |\nabla \xi| \rangle}, \qquad (8)$$

6

and we assume

$$D = 0.5 \ m^2/sec,$$

$$v = -2Dr/a^2;$$

r is a generalization of the minor radial coordinate. Here, r is defined as half of the width (the half-width) of a given flux surface on the midplane. It is thus a flux surface quantity. The neoclassical flux, Γ_j^{neo}, includes the Ware pinch for the hydrogenic components. The complete expressions are given in Ref. 5. These values for D and v are based loosely upon the TFTR simulations performed by Redi et al.[27] We have increased D by a factor of 5 to reduce the simulation time required for the profiles to reach steady state following an increase in density by gas puffing. We have also removed the impurity neoclassical contribution to D so as to obtain centrally peaked impurity density profiles soon after impurity influxing. The resulting steady-state profiles are consistent with those found in simulations not employing impurity influxing.

This transport model leads to centrally peaked electron density profiles when combined with an edge density that is much less than the volume average. Flat density profiles are obtained by removing the anomalous inward pinch ($v = 0$) and raising the pedestal boundary condition for the hydrogenic species to a value close to the volume-averaged density.

The only source term we will describe here is the impurity line radiation. It appears as a sink in the electron energy balance equation. The other contributions to Eqs. (5) and (8) are given in Ref. 5. For low temperature (< 2 keV), impure plasmas, the primary contribution to the radiative losses is from impurity line radiation. At low densities ($n_e < 10^{22} \ m^{-3}$), the plasma is transparent to its own radiation. Under these conditions, the electron collisional ionization rate can be balanced with the total recombination rate. Such systems are said to be in coronal equilibrium.[18,28] The result is an expression for the radiated power per unit volume of the form

$$p_{rad} = n_e n_z L_z(T_e), \tag{9}$$

where z indicates a particular impurity species. In addition to the function $L_z(T_e)$, one also obtains $\langle Z \rangle$ and $\langle Z^2 \rangle$ as functions of the electron temperature, T_e, only. These are the average values of the impurity charge and

its square in coronal equilibrium. In these simulations we will employ separately a high-Z impurity, titanium, and a low-Z impurity, carbon. We show in Figs. 1 and 2 plots of the formulas used[18,28] for $L_z(T_e)$ and $\langle Z \rangle$.

In general, coronal equilibrium is thought to be a good approximation when the plasma is stable in time, the neutral density is small. and the transport time scales are long relative to ionization and recombination time scales. Although these conditions are not likely to hold for a typical TFTR discharge, we utilize the coronal equilibrium model in the present work for simplicity. In preparing for detailed comparisons with experimental results in future work. we intend to upgrade the BALDUR code to account for some of the expected deviations from coronal equilibrium.[21]

Sawtooth oscillations in BALDUR are modelled using a Kadomtsev reconnection picture.[29,30] Of course, for there to be a reconnection, the safety factor on axis must be less than unity. When it is, the code periodically flattens the density and temperature profiles out to the mixing radius; there is no (direct) alteration of the exterior portion of the plasma. The value of the mixing radius is computed from the Kadomtsev theory.[30] It is typically 20 to 40% larger than the radius of the $q = 1$ surface. Since detailed models for the periodic trigger mechanism of the sawtooth oscillations are not available, the user is required to specify the period on input. For all of the simulations discussed here, it is fixed at 0.04 sec, typical of TFTR discharges exhibiting sawtooth oscillations.[27]

We wish to use this simulation model to fill out a Hugill diagram; that is, a plot of the maximum density attainable (normalized to B_T/R) as a function of $1/q_{cyl}$. Here, we use $q_{cyl} = 5a^2 B_T/RI_p$, where a and R are in m, B_T is in T, and I_p is in MA. We start each simulation with parameters such that the radiated power is well below the ohmic input power. After allowing a short period of time for the plasma to come to steady state (typically 2 sec), we make a small change in some parameter. Following this, we allow another second of simulation time for the system to return to a steady state. The parameter is then altered again, and so on until the code fails. In most cases, these failures are the result of exceeding a specified number of time steps. The time steps shorten considerably as the profiles contract.

In order to isolate the effects due to varying sawtooth mixing radii, we choose to scan $\bar{n}_e R/B_T$ at constant q_{cyl}. We use one of two procedures to carry out the scan. The easiest is to decrease I_p and B_T at constant I_p/B_T,

R, and $\overline{n_e}$. The other is to raise $\overline{n_e}$ by gas puffing. In order to keep n_z/n_e constant, we also influx an appropriate amount of the impurity species. In this way, Z_{eff} remains approximately constant. We define

$$Z_{eff} \equiv \frac{\sum_j n_j \langle Z_j^2 \rangle}{n_e},\tag{10}$$

where the sum is over all ionic species; their densities and charges are designated as n_j and $\langle Z_j^2 \rangle$, respectively. We will consider elsewhere the effects of allowing n_z/n_e to vary.[31]

For all of the simulations described here, the initial boundary conditions on the electron and ion temperatures at the plasma edge are of the pedestal type; typically, $T = 20$ eV. As the Murakami parameter, $\overline{n_e}R/B_T$, is increased, the amount of radiation relative to the input power increases, making it more difficult to maintain the edge plasma. At some point, the temperature of the computational zone just inside the boundary falls below the specified pedestal value. The presence of this positive gradient causes the code to switch to a zero energy flux boundary condition. Then, the edge temperature as a whole begins to fall, and the profile starts to contract.

We find that if $\overline{n_e}R/B_T$ is held fixed with a contracted profile, the plasma remains in a steady state. This mode of operation is reminiscent of the detached plasma experiments performed on TFTR.[32,33] At the edge of the computational boundary, one finds that the total radiated power equals the input (ohmic) power. In other words, the conducted and convected powers at the edge are effectively zero since $T \simeq 0$ and $dT/dr \simeq 0$ there.

Because the present BALDUR code does not contain a detailed mechanism for identifying the conditions under which the plasma should disrupt, we must use a more arbitrary criterion for defining the density limit in our simulations.

Of course, the simplest limit is the smallest $\overline{n_e}R/B_T$ for which the radiated power equals the input power. This would provide some interesting results, but would not tell the whole story. Namely, it is known that this is not a sufficient condition for a density limit disruption.[16,20,32,33] Restricting ourselves to this limit would also prevent us from utilizing some of the key features of a 1-1/2-D transport code. Namely, we would not be able to investigate the process of forming the contracted profiles, nor would be able to consider separately their stability (through the built-in equilibrium data).

The shape of the current profile in the vicinity of the $q = 2$ surface determines the stability of the $m = 2$, $n = 1$ tearing mode. This mode is thought to be instrumental in causing the observed disruption.[16,20,34] So, a reasonable disruption criterion can be based upon the degree to which the profiles near $q = 2$ are altered from their low radiation counterparts. For clarity, we choose to define a limit as that value of the Murakami parameter for which $T_e = 20$ eV at the $q = 2$ surface. In this way, virtually no current is flowing outside of the $q = 2$ surface.[16,20,35] It appears that a larger value for this critical temperature may be more appropriate.[36]

Another approach would be to plot the value of the internal inductance, ℓ_i, against q as the simulation evolves. Cheng, Furth, and Boozer[37] have computed stability boundaries in this space for external kink and tearing modes in circular cross section cylinder geometry. Their results could be used to define a more theoretically precise disruption limit. However, without more calculations of the same sort for elongated geometries, it would be difficult to generalize this criterion to CIT and the various reactor designs. Furthermore, only recently has an appropriate diagnostic for ℓ_i been installed in BALDUR. Most of the simulations discussed in this paper were performed prior to this upgrade.

In the future, a saturated tearing mode package,[22] currently being installed in BALDUR, will be utilized. By looking at the widths of the islands present, we might be able to arrive at a physically reasonable disruption limit. For now, we find it most convenient to define the density limit as occurring when $T_e = 20$ eV at the $q = 2$ surface. In addition to the above reasons, we prefer this procedure since it allows a precise definition of the critical Murakami parameter. However, it was necessary to use $T_e = 200$ eV in the carbon impurity runs in order to compare uniformly all of the data. Some of these terminated prior to satisfying the original criterion.

In all of our simulations, we employ a TFTR geometry: $R = 2.57$ m and $a = 0.82$ m. For our baseline parameters, we take $I_p = 2.2$ MA, $B_T = 4.7$ T, and $\overline{n_e} = 4.7 \times 10^{19}$ m^{-3}. These values are typical of TFTR low-q, ohmic discharges.[27] The actual plasma current, magnetic field, and electron density will vary from simulation to simulation.

The initial gas fill is mostly deuterium and hydrogen in a 9:1 ratio. In each run we use either titanium or carbon as the impurity species. When $\overline{n_e}$ is held fixed (or increased), gas puffing of the hydrogenic species in the 9:1

ratio offsets diffusive losses. The code is set up with a zero flux boundary condition on the impurity species so that their number is conserved in the absence of user-specified influx.

III. Results

In Table I, we show the various parameters for each of the runs and the line-averaged electron density, plasma current, magnetic field, and Murakami parameter at the time the disruption criterion is satisfied. All of the runs in the 02 and 03 series employ a titanium impurity. Carbon is used in 05 and 06. Because the changes in the temperature affect the average charge state of the impurity, it is difficult to assign a precise value of Z_{eff} to each run. For the runs with titanium, $Z_{eff} \simeq 1.1 - 1.2$; with carbon, $Z_{eff} \simeq 4 - 5$. Less titanium can be tolerated as a result of the bigger and broader (in temperature) peaks in the $L(T_e)$ curves shown in Fig. 1.

The runs 02d, 02f, 02g, and 02h form a q_{cyl} scan with peaked density profiles. Similarly, 02i, 02j, 02k, and 02l form a q_{cyl} scan with flat density profiles. For all other situations, just two different values of q_{cyl} are used to determine the scaling of the critical Murakami parameter. We show our results graphically in Fig. 3, where we plot $\overline{n_e}R/B_T$ vs. $1/q_{cyl} \propto I_pR/B_T$. The primary result is that with flat profiles $\overline{n_e}R/B_T$ depends weakly on q_{cyl}, whereas just the opposite is true for the peaked profile runs. We also display in Fig. 3 lines given by the scalings $\overline{n_e} = B_T/Rq_{cyl}$ and $\overline{n_e} = 2B_T/Rq_{cyl}$. Many of the present day estimates for the density limit scaling fall between these two lines (see, for example, Refs. 10 and 11).

As an example of how the electron temperature profile varies with simulation time (i.e., with the Murakami parameter), we show $T_e(r,t)$ from simulation 02h in Fig. 4. The contraction with incremental increases in the Murakami parameter (due here to decreases in B_T and I_p) is clear. The central temperature drops steadily as well. Some variation in the center due to sawtooth oscillations is apparent in Fig. 4, but the profiles remain relatively flat inside of the mixing radius at all times. At $t = 8.0$ sec in 02h, $T_e = 35$ eV at the $q = 2$ surface ($r \simeq 0.55$ m). By the end of the run, the electron temperature at that radius is well below 10 eV. The critical parameters of Table I are obtained by interpolating between these two steady states, so that there is no set of profiles corresponding exactly to our disruption criterion.

In Fig. 5. we plot the toroidal current density as a function of time and radial half-width for simulation 03d. Note that since this run is a density scan, the total plasma current is held fixed at 2.2 MA. As the temperature profile contracts, so does the current profile. The effect of each incremental addition to the density is evident as the edge of the current profile moves further in. The relatively frequent sawtooth oscillations cause the current density to be more or less flat in the center throughout the simulation. Note that at the end of this run, the $q = 2$ surface is near $r = 0.6$ m. and the sawtooth mixing radius is approximately $r = 0.4$ m. Figure 5 clearly shows that virtually all of the current is inside the $q = 2$ surface by the end of the simulation. indicative of an unstable profile. Our disruption criterion is actually met prior to this point. In particular. $T_e \simeq 30$ eV at $t = 6.5$ in this run. Again, the value of $\overline{n_e}$ given in Table I is obtained by interpolating between this state and the one found at the end of the simulation.

In Fig. 6, we present typical electron density profiles from two runs using a titanium impurity. The peaked profile comes from 02h. and the flat one is taken from 02l. In both cases, the sawtooth mixing radius is ~ 0.3 m. We should point out that even with the inward pinch, the variations in the density profile during the sawtooth rise are relatively minor. Furthermore. when the titanium impurity is used, the changes in its overall shape as other parameters (I_p, B_T, and $\overline{n_e}$) are varied are minimal. This is true even for states with severely contracted temperature profiles.

Figure 7 contains a plot of the electron density as a function of time and radial half-width for simulation 06e. This is a flat profile I_p, B_T scan with carbon impurity. Note that as the contraction proceeds the central density increases to maintain constant $\overline{n_e}$. The carbon density profile remains flat throughout. The contraction is the result of the reduction in $\langle Z \rangle$ of carbon in the outer zones as the local electron temperature falls with time (see Fig. 2). This effect is not apparent in the titanium runs because of the much lower contribution to n_e made by the impurity, $\langle Z \rangle n_z$. Note that with Eq. (10), $\langle Z \rangle n_z \simeq (Z_{eff} - 1)/(\langle Z \rangle - 1)$. So. there is less electron density due to the impurity in the titanium runs than in the carbon runs because of the lower Z_{eff} and the higher $\langle Z \rangle$.

The radiated power per unit volume [i.e., Eq. (9)] as a function of time and radial half-width for simulation 02h is displayed in Fig. 8. The contributions from the primary (low temperature) and secondary peaks of $L(T_e)$ are clear

(see Fig. 1). Note that even with constant line-averaged electron density the magnitude of the primary peak increases as the contraction progresses. This is just due to the higher electron and impurity densities at the smaller radii. One effect that is not clear in Fig. 8 is the change in the radial width of the peaks as the temperature profile steepens. In particular, a steeper (more contracted) temperature profile leads to a narrower peak in the radiated power since the width of $L(T_e)$ in temperature space is fixed. The total radiated power is given by:

$$P_{rad} = 4\pi^2 R \int_0^a r dr n_e n_z L[T_e(r)].$$ (11)

In this expression, a steeper temperature profile leads to a smaller dr for a given dT_e. Furthermore, because of the contraction, the factor r is smaller as well. Thus, in the contracted state the reductions in the volume element, rdr, corresponding to a given peak in $L(T_e)$ can counteract to some extent the increased densities, and the total radiated power does not vary so much. These effects are critical to understanding why the maximum Murakami parameter for the simulations scales as shown in Fig. 3. We will clarify these points in Sec. IV.

As pointed out in Sec. II, the flat profile runs are obtained by removing the anomalous inward pinch from the particle transport model and setting the edge density close to the volume average (e.g., Fig. 6). This implies that $n_e n_z$ in the low temperature ($T_e < 100$ eV) region is much larger than it is for peaked profiles with the same volume-averaged density. Consequently, if all other factors are the same, the total radiated power is greater with flat profiles. In choosing the initial conditions for the flat profile runs, we took this into account. With titanium, we just lowered the impurity concentration relative to that used in the peaked profile cases. In 06c and 06e, the two carbon runs with flat profiles, we reduced $\overline{n_e}$, as indicated in Table I. In Fig. 8, the radiated power per unit volume increases as the contraction of the temperature profile progresses due to the peaked profiles. With flat profiles, however, the radiated power per unit volume remains approximately constant as the simulation proceeds. This is demonstrated in Fig. 9, taken from 02j. In cases such as this, the total radiated power tends to decrease with increasing Murakami parameter due to the volume element shrinkage noted above.

We feel that these effects are connected directly to the scaling of the critical $\overline{n_e} R / B_T$ with q_{cyl} noted in Fig. 3. The crucial point is to realize that

13

as q_{cyl} is increased, the $q = 2$ surface moves closer to the magnetic axis and. thus. to regions of higher density, assuming a fixed, peaked density profile. At our defined point of disruption, the radiation peaks near the $q = 2$ surface. For the higher q_{cyl} runs, the radiation per unit volume at this point is larger simply because the density is larger. In some sense, this requires a higher ohmic heating power to maintain thermal equilibrium. Since P_{OH} increases with B_T/R, this requirement translates to a smaller maximum Murakami parameter.

We should also point out that the initial points for the runs comprising a q_{cyl} scan are. in the 02 series for example, $I_p = 2.2$ MA and $\overline{n_e} = 4.7 \times 10^{19}$ m^{-3}, with B_T computed from q_{cyl}. For the peaked profile runs in this series, it is clear that P_{OH}/P_{rad} increases with q_{cyl} while P_{OH} remains almost constant. Again, the reason for this is the effect of the density profile shape on P_{rad}. Hence, our reasoning does not apply just to conditions at disruption.

This analysis can easily be generalized to the case where the volume-averaged density is allowed to vary for fixed current and toroidal field if the density profile remains fixed. We will quantify these arguments in the next section.

IV. Analytic Calculations

We now attempt to demonstrate analytically how the scalings noted in Fig. 3 might arise. These calculations will be carried out within the confines of our model, the limitations of which have already been noted. Previous theoretical studies have yielded scalings for the maximum Murakami parameter independent of current,[17] as well as a scaling of the maximum density with current (i.e., a Hugill limit) by the introduction of various physical effects.[13,14,16,20] Rebut and Green,[13] for example, relied in part on the scaling of neoclassical transport coefficients to obtain a variation in the Murakami parameter with q. Ohyabu[14] found a q scaling via its effect on the temperature in ohmic equilibrium. The result presented by Campbell et al.[20] employs an empirical scaling for the radiation that has q_{cyl} dependence in the volume of the radiating layer (and implicitly through the input power). The work presented in Ref. 16 perhaps most closely resembles that discussed in Sec. III. Roberts[16] included the effects of a density gradient when computing the radiation. The contracted current profiles were examined for tea. ng mode stabil-

ity in order to identify disruptive conditions. As in our Fig. 3. Roberts found that the critical Murakami parameter increased with decreasing q_{cyl}. Their calculation lacked, however. self-consistently computed current and density profiles, and did not explicitly include the effects of sawtooth oscillations.

We will show how the presence of a density gradient can lead to a variation of the Murakami parameter with q_{cyl}; for these purposes, $q_{cyl} = 5a^2 B_T / R I_p$, where R and a (the full simulation minor radius) are in m, B_T is in T, and I_p is in MA. Since the sawtooth oscillations are instrumental in determining the radial transport in these simulations, we find it necessary and even convenient to include their effects here. In general, the line of reasoning used in our calculations is motivated by the detailed results of our simulations. While this limits us to the models assumed therein, it also allows us to check intermediate expressions. insuring a thorough understanding of the phenomena appearing in the simulations.

In order, we will present formulas for the central electron temperature, the radiated power and the ohmic heating power. Then, by equating the radiated power to the ohmic heating power under the conditions assumed to hold at disruption ($T_e = 20$ eV at $q = 2$), a scaling for the critical density can be obtained. Unless otherwise specified, all units are MKS, and temperatures are in keV.

We will assume circular flux surfaces and steady state in what follows. Consider first the interior portion of the plasma where the radiated power is negligible. Then, integrating the radial power balance out to the sawtooth mixing radius, we obtain:

$$r \left(n_e \chi_e \frac{dT_e}{dr} + n_i \chi_i \frac{dT_i}{dr} \right) \Bigg|_{r_{mix}} = \int_0^{r_{mix}} r \, dr \, p_{OH}, \qquad (12)$$

where $p_{OH} = \eta_{\parallel} J^2$ is the ohmic heating power density. We have applied the boundary condition $dT/dr(r = 0) = 0$. The parallel resistivity can be written as

$$\eta_{\parallel} = 1.65 \times 10^{-9} Z_{eff} \ln \Lambda \gamma_{NC} T_e^{-3/2}, \qquad (13)$$

with $\ln \Lambda$ representing the Coulomb logarithm and γ_{NC} the neoclassical resistivity enhancement.[38]

In Eq. (12), the toroidal current density is denoted by J. Due to the action of the frequent sawteeth, both J and T_e are approximately constant

15

over $0 \leq r \leq r_{mix}$ (see Figs. 4 and 5). In particular, we can use for J its value at the magnetic axis.

$$J \simeq J_0 = \frac{2B_T}{\mu_0 R q_0}. \tag{14}$$

Furthermore, we will assume from here on that the safety factor on axis is unity, $q_0 = 1$.

To evaluate the gradients on the left-hand side of Eq. (12) in general, we need to know the profile shape. With the sawtooth oscillations, we expect a scaling like

$$\frac{dT_e}{dr}(r > r_{mix}) \simeq -\left(\frac{T_{e0}}{a - r_{mix}}\right), \tag{15}$$

where T_{e0} is the central temperature. We then assume

$$\frac{dT_i}{dr} \simeq \frac{T_{i0}}{T_{e0}} \frac{dT_e}{dr}. \tag{16}$$

As in our simulations, we use an electron thermal diffusivity

$$\chi_e = \frac{2.6 \times 10^{19}}{n_e}, \tag{17}$$

with $\chi_i = \chi_e/2$.

Given these assumptions, Eq. (12) yields

$$T_{e0} = 0.76 \left[\frac{r_{mix}(a - r_{mix})}{\left(1 + \frac{1}{2}\frac{n_i}{n_e}\frac{T_{i0}}{T_{e0}}\right)} \bar{\gamma}_{NC} Z_{eff} \ln \Lambda\right]^{2/5} \left(\frac{B_T}{R}\right)^{4/5}, \tag{18}$$

where

$$\bar{\gamma}_{NC} \equiv \frac{2}{r_{mix}^2} \int_0^{r_{mix}} r \, dr \, \gamma_{NC}(r) \tag{19}$$

accounts for the principal radial variation of the ohmic heating power density out to the mixing radius. Equation (18) does a good job of reproducing the values for the central temperature found in the simulations provided the minor radius, a, is taken to be the radius at which $T_e = 20$ eV. This is necessary to obtain a reasonable estimate of the temperature gradient found in Eq. (12). Some inaccuracy is allowable here due to the weak dependence of T_{e0} on dT_e/dr.

16

In general, the total radiated power is given by Eq. (11). Once the plasma is detached, the low temperature peaks of $L(T_e)$ should provide the largest contribution to P_{rad} (see Fig. 1). This is true for both the low-Z and the high-Z impurities we consider here. So, it is reasonable to approximate $L(T_e)$ by

$$L(T_e) = \begin{cases} L_p, & T_1 < T_e < T_2, \\ L_s, & T_3 < T_e < T_4, \\ 0, & \text{otherwise}, \end{cases} \qquad (20)$$

where $T_1 < T_2 < T_3 < T_4$ and $L_p > L_s$. We define corresponding radii, $r_j \equiv r(T_j)$ for $j = 1, 4$. We include two peaks in Eq. (20) in order to improve the quantitative accuracy of the resulting expression. With just one peak, however, the fundamental scaling obtained will be essentially the same. In fact, the procedure could be extended to include an arbitrary number of peaks, but we find that Eq. (20) suffices for present purposes. Looking at the plot in Fig. 1, we estimate $T_1 = 20$ eV, $T_2 = 100$ eV, $T_3 = 300$ eV, $T_4 = 600$ eV. $L_p = 2.5 \times 10^{-31}\ Wm^3$, and $L_s = 5.0 \times 10^{-32}\ Wm^3$ for titanium.

These peaks are relatively narrow in terms of electron temperature. With non-zero temperature gradients, they correspond to small intervals in radius. We can thus reasonably approximate the total radiated power by

$$P_{rad} \simeq 2\pi^2 R \left\{ L_p \left(r_1 - r_2 \right) \left[r_1 n_e(r_1) n_z(r_1) + r_2 n_e(r_2) n_z(r_2) \right] \right. \\ \left. + L_s (r_3 - r_4) \left[r_3 n_e(r_3) n_z(r_3) + r_4 n_e(r_4) n_z(r_4) \right] \right\}. \quad (21)$$

The total ohmic input power is given by

$$P_{OH} = 4\pi^2 R \int_0^a r\, dr\, \eta_\parallel J^2. \qquad (22)$$

If the parallel electric field, $E_\parallel = \eta_\parallel J$, is constant over the minor radius, $P_{OH} = (2\pi R) E_\parallel I_p = I_p V_{loop}$, where V_{loop} is the loop voltage. We already know $\eta_\parallel$ and J at $r = 0$. Inserting these expressions into Eq. (22) yields a viable scaling for P_{OH}. However, the combination of neoclassical resistivity and our model for the sawtooth oscillations leads to variations in $E_\parallel = \eta_\parallel J$ over $0 < r < r_{mix}$. Namely, if both $J(r)$ and $T_e(r)$ flatten in this region following a sawtooth crash, $E_\parallel \propto \gamma_{NC}(r)$. Since the sawtooth period is much less than the resistive skin time, $E_\parallel$ remains peaked off-axis at all times.[39] On the other hand, for $r > r_{mix}$, $E_\parallel$ is approximately independent

17

of radius in our simulations. Inserting a correction factor to account for the variation of γ_{NC} inside the sawtooth mixing radius and using Eq. (13), $P_{OH} \propto (2\pi R)E_\parallel(r=0)I_p$ yields

$$P_{OH} = 0.0165\, Z_{eff} \ln \Lambda [0.9\gamma_{NC}(r_{mix})](B_T I_p T_{e0}^{-3/2}). \tag{23}$$

The factor of 0.9 represents an attempt to calibrate this formula using data from our simulations. The resulting expression predicts the ohmic heating power under all conditions to within about 10% (using the observed T_{e0}).

In order to estimate the various radii appearing in Eqs. (18), (21), and (23), we now specialize to the conditions at disruption; namely, $T_e = 20$ eV at the $q = 2$ surface. This corresponds to a highly contracted current profile, $J \simeq 0$ for $r > r_{mix}$. But, $J \simeq J_0$ for $0 < r < r_{mix}$. Since we know the total current, we can write

$$r_{mix} \simeq 0.94 \left(\frac{\mu_0}{2\pi} \frac{I_p R}{B_T}\right)^{1/2}; \tag{24}$$

the factor of 0.94 arises from matching with the simulation results (i.e.. allowing for a slightly broader current profile in reality).

In general, the temperature profile in a contracted state flattens dramatically for $r > r_1 \equiv r(T_e = T_1)$ because of the relatively small amount of heat flow past the primary radiation peak. So, we can reasonably characterize the temperature profile by setting the plasma minor radius $a = r_1$. As noted previously, this a just serves to estimate the temperature gradient in Eq. (18). For titanium, we take $T_1 = 20$ eV, so that $r_1 = r(q = 2) = r(T_e = 20\,\text{eV})$ when the disruption criterion is satisfied. We suggest that this equality will hold for a general impurity as long as $T_1 \ll T_{e0}$. Even if this requires a redefinition of the disruption criterion in order to be consistent (such that $T_e = T_1$ at $q = 2$, for example), the following scalings should still be valid.

Given that the assumption of $J \simeq 0$ for $r > r_{mix}$ works well in Eq. (24), it should work even better in calculating $r(q = 2)$. In a circular cylinder geometry, the equalities suggested above lead to

$$a = r_1 = r(q = 2) = \left(\frac{\mu_0}{\pi} \frac{I_p R}{B_T}\right)^{1/2}. \tag{25}$$

18

To obtain the other radii appearing in Eq. (21), we need to further specify the temperature profile. We will assume

$$T_e(r) = \begin{cases} T_{e0}, & 0 < r < r_{mix}, \\ (T_{e0} - T_{ea}) \left(\frac{a-r}{a-r_{mix}}\right)^{\alpha_T} + T_{ea}, & r_{mix} < r < a. \end{cases} \tag{26}$$

Then,

$$r(T_j) = a - (a - r_{mix}) \left(\frac{T_j - T_{ea}}{T_{e0} - T_{ea}}\right)^{1/\alpha_T}. \tag{27}$$

If we define the edge temperature, $T_{ea} = T_e(a)$, to be equal to T_1 as would follow from the above discussion, this formula holds for $j = 1$ as well as $j = 2 - 4$. For simplicity, we will neglect T_{ea} relative to T_{e0} in using Eq. (27).

We expect in general that the temperature profile exponent α_T will be in the range 1 - 2. Using dT_e/dr near the edge (i.e., between r_1 and r_4) from several simulations to estimate α_T, we find $\alpha_T \sim 1.4$. However, we retain α_T in the following expressions for completeness.

Setting $P_{rad} = P_{OH}$, and making use of Eqs. (18), (24), (25), and (27), we obtain

$$\left(\frac{B_T}{R}\right)^{\frac{3}{10} + \frac{1}{\alpha_T}\frac{2}{5}} I_p^{-\frac{1}{10} - \frac{1}{\alpha_T}\frac{2}{5}} =$$

$$\frac{44.}{(0.29)^{1/\alpha_T}} \left[\frac{\overline{\gamma}_{NC}/\gamma_{NC}(r_{mix})}{\left(1 + \frac{1}{2}\frac{n_i}{n_e}\frac{T_{i0}}{T_{e0}}\right)}\right]^{\frac{3}{5} - \frac{1}{\alpha_T}\frac{2}{5}}$$

$$\times \left[\gamma_{NC}(r_{mix})Z_{eff} \ln \Lambda\right]^{-\frac{2}{5}\left(\frac{\alpha_T+1}{\alpha_T}\right)} \langle L\Delta T r n_e n_z \rangle, \tag{28}$$

where I_p is now in MA. We have defined

$$\langle L\Delta T r n_e n_z \rangle \equiv L_p (T_2 - T_{ea})^{1/\alpha_T} \left[r_1 n_e(r_1) n_z(r_1) + r_2 n_e(r_2) n_z(r_2)\right]$$
$$+ L_s \left[(T_4 - T_{ea})^{1/\alpha_T} - (T_3 - T_{ea})^{1/\alpha_T}\right]$$
$$\times \left[r_3 n_e(r_3) n_z(r_3) + r_4 n_e(r_4) n_z(r_4)\right]. \tag{29}$$

The only thing remaining to do is to determine the scaling of $\langle L\Delta T r n_e n_z \rangle$. We will assume

$$\langle L\Delta T r n_e n_z \rangle \propto \overline{n}_e^2 \frac{n_z}{n_e} q_{cyl}^p i \tag{30}$$

19

we need to estimate the exponent p. The q_{cyl} scaling comes in not only through the factors r_1 through r_4 e.g., as in Eq. (25), but also through the density profile, as discussed in Sec. III. Namely, as q_{cyl} is raised, the contraction must proceed to smaller radii in order to satisfy the disruption criterion. At these radii, the electron and impurity densities are higher (for peaked profiles). Hence, the density factors appearing in $\langle L\Delta Trn_e n_z \rangle$ increase with q_{cyl}. As pointed out in Sec. III, the overall shape of the profile in the cases with titanium impurity does not vary much when the plasma current and/or the toroidal field are changed. So, for the purposes of estimating p, we suppose that the density profiles are fixed.

From Eqs. (24) and (25), we know $r_{mix}, a \propto q_{cyl}^{-1/2}$; we assume for simplicity that this scaling is dominant in Eq. (27), $r_j \sim q_{cyl}^{-1/2}$. Then, we see that with flat profiles (no q_{cyl} scaling for the density factors), $\langle L\Delta Trn_e n_z \rangle \propto \overline{n_e}^2(n_z/n_e)q_{cyl}^{-1/2}$.

In the case of peaked profiles, write $n_e(r_j)n_z(r_j) \propto q_{cyl}^{p'}$, then

$$\frac{d}{dq_{cyl}}n_e n_z \propto \frac{p'}{q_{cyl}}n_e n_z. \tag{31}$$

Taking a profile shape analogous to Eq. (26), with exponents α_e and α_z for the electron and impurity density profiles, respectively, we obtain

$$\frac{d}{dq_{cyl}}\left[n_e(r_j)n_z(r_j)\right] = -\frac{dr_j}{dq_{cyl}}(\alpha_e + \alpha_z)\frac{n_e(r_j)n_z(r_j)}{(a_0 - r_j)}. \tag{32}$$

Because there is no contraction of the density profile, we employ a_0 here, the initial plasma minor radius in the simulations. Using $r_j \sim q_{cyl}^{-1/2}$ as suggested and referring to Eq. (31), we can determine a local effective exponent,

$$p' \sim \frac{\alpha_e + \alpha_z}{2}\frac{r_j}{a_0 - r_j}. \tag{33}$$

We expect $\alpha_e \sim \alpha_z \sim 1$. The scaling is likely to be dominated by that of the radii of the low temperature peaks, i.e., r_1 and r_2. Since these never get as small as $a_0/2$ during our simulations, it is reasonable to take $r_j/(a_0 - r_j) > 1$; we use $r_j/(a_0 - r_j) \sim 3/2$ for clarity. Thus, $p' \sim \frac{3}{2}$. With $r_j \sim q_{cyl}^{-1/2}$, we finally obtain

$$\langle L\Delta Trn_e n_z \rangle \propto \overline{n_e}^2\frac{n_z}{n_e}q_{cyl} \tag{34}$$

20

for peaked profiles.

Expressing q_{cyl} in terms of I_p and B_T/R. and considering just the overall scaling, Eq. (28) yields at fixed n_z/n_e

$$\overline{n}_{e,crit} \propto \left(\frac{B_T}{R}\right)^{\frac{9}{20} - \frac{1}{5\alpha_T} - \frac{p}{2}} I_p^{-\frac{1}{20} - \frac{1}{5\alpha_T} + \frac{p}{2}}. \tag{35}$$

Then, inserting $\alpha_T = 1.4$, and $p = -1/2$ for flat profiles, $p = +1$ for peaked profiles,

$$\overline{n}_{e,crit} \propto \begin{cases} \left(\frac{B_T}{R}\right)^{0.84} I_p^{-0.16}, & \text{flat profiles,} \\ \\ \left(\frac{B_T}{R}\right)^{0.09} I_p^{0.59}, & \text{peaked profiles.} \end{cases} \tag{36}$$

In Tables II and III, we apply this scaling to the results given in Table I. For comparison, we include in these tables the simplest scalings apparent in Fig. 3. For the peaked profile runs. it looks as though something like the familiar Hugill limit, $\overline{n}_e \propto I_p$, should apply, while for flat profiles $\overline{n}_e \propto B_T$ appears to be appropriate.

For the peaked profile cases, Eq. (36) works very well (i.e., the constant of proportionality in Table II does not vary much). Neither of the scalings listed in Table III does as good a job of explaining the flat profile data. One of the problems is that the density profiles are not completely flat (see Fig. 6). Furthermore, in the high q_{cyl} cases, the length of the scan is considerable. The number of points along the scan is fixed by code limitations, so that the error in estimating of the critical density is larger for these runs.

The preceding calculations should hold for the runs with carbon impurity as well apart from the estimated q_{cyl} scaling of $\langle L\Delta T r n_e n_z \rangle$. Because of the changes in the electron density profile accompanying the temperature profile contraction, it is not clear how this scaling can be determined. On the other hand, the trends apparent in Fig. 3(c) are similar to those found in the simulations with titanium impurity. Namely, with peaked density profiles, $\overline{n}_{e,crit}$ still scales approximately like the total current; but with flat profiles, the scaling is reduced. We suspect that the effects responsible are similar, but obscured by the contraction of the electron density profile.

V. Discussion and Conclusions

In this section, we comment on how our results relate to experimental observations. But, first, it is appropriate to point out the shortcomings of the present model and to indicate how they impact our results. For instance, the fact that the data of Fig. 3 fall well within the range of present empirical scalings (for example,[11] $\overline{n_e} < 2B_T/Rq_{cyl}$) is somewhat coincidental. This is because we have taken no steps to determine self-consistently the impurity concentration in these simulations. In all cases it is specified arbitrarily on input. Since the radiated power is directly proportional to the impurity density, we could extend our results to larger Murakami parameters just by lowering n_z/n_{e_1} as has been noted previously.[9,10,15,17] The effect is offset somewhat, but not completely by the increase in the ohmic power with Z_{eff} as is evident in Eq. (28).

Our model is also inadequate in that coronal equilibrium is known to under-predict the radiation in actual experiments.[19] By assuming coronal equilibrium, we omit effects such as charge exchange recombination of impurities[21,40] (significant in the presence of high neutral density) and transport of individual impurity charge states on time scales shorter than those over which coronal equilibrium is established. Roberts[16] points out that including the latter effect leads to smaller critical Murakami parameters, particularly for low Z impurities. Heuristic corrections to the coronal equilibrium model would improve the accuracy of our results to some extent, but would not aid in formulating the general, predictive model that we seek.

Lastly, our disruption criterion is arbitrary. It may not be inadequate, however, especially for the present scaling arguments. Our guideline is effectively the same as that used by Perkins and Hulse.[17] They define the density limit as the point at which $P_{rad} = 0.8P_{OH}$ when evaluated at $q = 2$. Since most of the radiation in our runs comes from the low temperature part of the profile, $T_e < 100$ eV, we do not satisfy their condition until the temperature profile contracts inside of $q = 2$. However, at this point our disruption criterion ($T_e = 20$ eV at $q = 2$) is nearly satisfied. Preliminary indications are that use of the stability boundary in ℓ_i vs. q space given by Cheng et al.[37] yields nearly equivalent results.

The procedure used by Roberts[16] represents the next level of sophistication. In Ref. 16, the profiles resulting from an electron energy balance are

analyzed for tearing mode stability, yielding saturated island widths. The disruption mechanism discussed there most closely resembling the criterion we employ is due to the interaction between the 2/1 tearing mode and the cold plasma outside the radiating boundary. It appears that the widths of the islands in their work do not change greatly as conditions are varied. If this really is the case, then improving our disruption criterion involves only redefining the surface ($q > 2$) that must be reached by the cold plasma. The basic scalings arrived at above should still hold. The tearing mode package being installed in BALDUR[22] will be able to not only calculate saturated island widths, but will also treat self-consistently the effects of localized current profile flattening.

For the purposes of identifying the basic scaling of the density limit in ohmic discharges, our model should be adequate. In particular, the effects of density gradient and sawteeth we treat here do lead to interesting results that are not likely to be affected by the above-mentioned shortcomings.

We now compare our results with some specific experimental observations. First, we consider the density limit formula presented in Ref. 20:

$$\bar{n}_{e,crit}^{-JET} = 3.5 \times 10^{19} \left[\frac{P q_{cyl}}{(Z_{eff} - 1) R \kappa a^2 (q_{cyl} - 2/\kappa)} \right]^{1/2} , \qquad (37)$$

where P is the total input power in MW, and κ is the plasma elongation ($\kappa \simeq 1$ for a TFTR geometry). This relation is obtained by equating an empirical scaling for the radiated power with the input power. Equation (37) applies only if Z_{eff} is not close to one and if light impurities (e.g., oxygen and carbon) dominate the radiated power. All of our runs with carbon impurity fall into this category. Inserting $P = P_{OH}$ and Z_{eff} for a particular time during each simulation, we find that on the average $\bar{n}_e / \bar{n}_{e,crit}^{-JET} \sim 2$, where $\bar{n}_e$ is taken as in Table I. Because of the variations in P_{OH} and Z_{eff} during our runs, $\bar{n}_{e,crit}^{-JET}$ cannot be uniquely determined. It is fairly clear that $\bar{n}_{e,crit}^{-JET}$ does not exhibit the same current scaling as displayed in Fig. 3(c). Namely, for each pair of runs with carbon impurity (05b and 05c, for example), the $\bar{n}_e$ at the two different values of q_{cyl} in Table I is either similar, or defined to be the same (I_p, B_T scans). Yet, their formula predicts a noticeable variation with q_{cyl} in all cases, as is clear from Eq. (37). The source of this discrepancy is uncertain.

The fact that the critical densities predicted by our model are about a

factor of two below those found with Eq. (37) indicates that the magnitude of the radiation obtained using coronal equilibrium is approximately four times smaller than that observed experimentally e.g., see Eq. (28). This is consistent with the calculation presented in Ref. 19, where the coronal equilibrium radiation is a factor of five to ten smaller than that computed from the radiation data.

In gas-fuelled, ohmic discharges, TFTR has obtained Murakami parameters up to[23] $\bar{n_e}R/B_T = 3.2 \times 10^{19}$. In present TFTR shots, the dominant impurities are carbon and oxygen. From Table I, we see that the maximum value in our runs is $\bar{n_e}R/B_T = 5.66 \times 10^{19}$ (from 06a). This discrepancy is again consistent with our underestimating the radiation by about a factor of four. On the other hand, pellet injection into TFTR yields much higher densities, $\bar{n_e} = 1.4 \times 10^{20}$ and $\bar{n_e}R/B_T = 6.5 \times 10^{19}$. This indicates the importance of fuelling and recycling effects;[23] they will be the focus of future investigations.[31]

The detached plasmas studied in TFTR[32,33] are very similar to the steady-state contracted plasmas investigated here. Because these TFTR discharges remain in the detached state for many energy confinement times without disrupting, they serve as a source of experimental data with which we can compare and calibrate our model. For now we would just like to point out some of the similarities between the simulations presented here and the experiments discussed in Refs. 32 and 33. Much as we have done, the detached plasmas in TFTR are produced by ramping down the current at constant line-integrated density. It is convenient for us to also ramp down the toroidal field in order to maintain a constant q_{cyl}.

Experimentally, the resulting detached plasma has a contracted temperature profile ($T_e < 50$ eV in the cold edge region), bounded by a radiating layer. The electron density profile also appears to be somewhat contracted.[33] The power balance calculations reported by Strachan et al.[33] indicate that all of the ohmic power appears as radiated power; that is, there is little or no heat conducted or convected to the limiter. All of these features are consistent with our simulations employing a carbon impurity.

There are several other trends mentioned in Ref. 33 that are reminiscent of behaviors found in our simulations. First, a decrease in the effective minor radius (defined via the temperature profile) can be brought about by either increasing the central electron density or decreasing the plasma current. An

24

experimental scaling for this has been determined:

$$a \propto I_p^{0.64 \pm 0.05} n_e(0)^{-0.3 \pm 0.04}. \tag{38}$$

The data with carbon impurity we have presented are not extensive enough to allow a detailed comparison with this expression, but preliminary indications are that our simple model yields a weaker current scaling than this.

Secondly, the total radia' : power and the radiated power per unit volume increase with central electron density both in the experiments and in our simulations. We cannot say anything definite about how these quantities vary with plasma current in our runs because of the increases in central density that are required during the profile contraction to maintain constant line-averaged density (see Fig. 7) in the I_p, B_T scans. We do note that in run 06e, the total radiated power decreases with plasma current, despite an increase in $n_e(0)$ (see Fig. 7). In Ref. 33 it is noted that the central electron temperature falls as the central density is increased. This is also the case for our two density scans with carbon impurity (05b and 05c).

Finally, Strachan et al.[33] point out that the safety factor at the effective edge of the plasma decreases with increasing $n_e(0)$, down to about $q = 2$. Further attempts to increase the central density lead to disruption. This is another indication that our disruption c 'terion, $T_e = 20$ eV at $q = 2$, is reasonable. Future work will attempt to make more quantitative comparisons between the simulations and experiments.

In summary, we have developed a relatively simple transport model that yields qualitatively correct scalings for the density limit in ohmic tokamak discharges. The emphasis here has been on effects of the density profile. In particular, we have pointed out that at constant line-averaged electron density, a flat profile generates more radiated power than a peaked profile just due to the higher edge density.

The profile shape also impacts the current scaling of the critical electron density. Namely, with peaked electron density profiles, the location of the $q = 2$ surface moves inward to regions of higher density as q_{cyl} is raised. This leads to an effectively higher radiated power than at smaller q_{cyl} in the maximally contracted state where the peak of the radiation is near $q = 2$. This is also true of the initial, uncontracted states used in our simulations. The end result is a decrease in the allowable Murakami parameter as q_{cyl} is increased. Of course, the argument does not hold for flat profiles, and very

little scaling of the Murakami parameter with q_{cyl} is noted in those cases. These trends are clear in Fig. 3 and have been confirmed by our analytic calculations.

These two density profile effects suggest that if all other factors (impurity concentration, average density, etc.) are the same, discharges with peaked profiles will yield larger critical Murakami parameters than those with flat profiles. So, in an actual experimental data base consisting of a large number of shots produced under various conditions, the ones yielding the highest Murakami parameter at a given q_{cyl} will be the ones with the most peaked profiles.

It has been observed experimentally that Z_{eff} decreases with increasing density.[23] We have not taken this into account in our simulations (we keep Z_{eff} approximately constant as the density is varied). It would act to enhance the q_{cyl} scaling of the maximum Murakami parameter shown in Fig. 3. For example, if we write instead of Eq. (30)

$$\langle L\Delta T r n_e n_z \rangle \propto \overline{n_e} n_z q_{cyl}^p \tag{39}$$

and hold n_z constant, the exponents in Eqs. (35) and (36) double. Then, the scaling of $\overline{n}_{e,crit}$ with current is stronger, but still close to linear. In this way, our relatively simple model can account for the overall shape of the Hugill diagram.

The effects of pellet injection and auxiliary heating will be examined in the near future.[31] The importance of profile shape indicates that the central fuelling that can be provided by pellet injection allows higher line-averaged densities to be attained. This result is clear in present experiments.[10,11,23] Peaked profiles are of even greater importance in a reactor due to their impact on the fusion power output.[1,3] It is also known that auxiliary heating can increase the maximum allowable Murakami parameter.[9-11] Clearly, our model will yield this result since it is based upon a radiative power balance. Greenwald[9,10] has proposed that mechanisms insensitive to input power and impurity concentration may actually be responsible for the current scaling of the density limit. Future work will attempt to clarify this picture.

Our next step in developing a predictive model for the density limit will be improving the radiation model in the BALDUR code, allowing it to treat effects such as charge exchange recombination[40] and transport of impurity charge states.[21] Attempts will also be made to treat the scrape-off layer and

boundary conditions in a more realistic fashion (see, for example, Ref. 41). These steps will be undertaken with guidance from experimental data.

Acknowledgments

References

[1] D. P. Stotler. D. Post, and G. Bateman, Princeton Plasma Physics Laboratory Report No. PPPL-2463 (1987); Fusion Technol. (in press).

[2] D. Post, W. Houlberg, G. Bateman, L. Bromberg, D. Cohn, P. Colestock, M. Hughes, D. Ignat, R. Izzo, S. Jardin, C. Kieras-Phillips, L. P. Ku, G. Kuo-Petravic, B. Lipschultz, R. Parker, C. Paulson, Y-K. M. Peng, M. Petravic, M. Phillips, N. Pomphrey, J. Schmidt, D. Strickler, A. Todd, N. Uckan, R. White, S. Wolfe, and K. Young, Physica Scripta **T16**, 89 (1987).

[3] D. P. Stotler and Glenn Bateman, Princeton Plasma Physics Laboratory Report No. PPPL-2510 (1988); Fusion Technol. (to be published).

[4] S. M. Kaye and R. J. Goldston, Nucl. Fusion **25**, 65 (1985).

[5] C. Singer, D. Post, D. Mikkelsen, M. Redi, A. McKenney, A. Silverman, F. Seidl, P. Rutherford, R. Hawryluk, W. Langer, L. Foote, D. Heifetz, W. Houlberg, M. Hughes, R. Jensen, G. Lister, and J. Ogden, Princeton Plasma Physics Laboratory Report No. PPPL-2073 (1986); Comput. Physics Commun. (in press).

[6] G. Bateman, in *Proceedings of the 1985 Trieste Spring College on Plasma Physics* (to be published).

[7] M. Murakami, J. D. Callen, and L. A. Berry, Nucl. Fusion **16**, 347 (1976).

[8] K. B. Axon, W. H. M. Clark, J. G. Cordey, M. Cox, S. J. Fielding, R. D. Gill, J. Hugill, P. Lomas, J. W. M. Paul, B. A. Powell, R. Prentice, D. F. Start, D. D. R. Summers, and P. Thomas, in *Plasma Physics and Controlled Nuclear Fusion Research 1980*, Proceedings of the 8th International Conference, Brussels, (IAEA, Vienna, 1981), Vol. 1, p. 413.

[9] M. Greenwald, M. Besen, F. Camacho, C. Fiore, M. Foord, R. Gandy, C. Gomez, R. Granetz, D. Gwinn, S. Knowlton, B. LaBombard, B. Lipschultz, H. Manning, E. Marmar, S. McCool, J. Parker, R. Parker, R. Petrasso, P. Pribyl, J. Rice, D. Sigmar, Y. Takase, J. Terry, R. Waterson, and S. Wolfe, in *Plasma Physics and Controlled Nuclear Fusion Research*

1986, Proceedings of the 11th International Conference, Kyoto (IAEA, Vienna, 1987), Vol. 1, p. 139.

[10]M. Greenwald, J. Terry, S. Wolfe, S. Ejima. M. Bell, S. Kaye, and G. H. Neilson, MIT Plasma Fusion Center Report No. PFC/JA-86-22 (1988).

[11]JET Team, in *Plasma Physics and Controlled Nuclear Fusion Research 1986,* Proceedings of the 11th International Conference, Kyoto (IAEA, Vienna, 1987), Vol. 1, p. 31.

[12]A. Gibson, Nucl. Fusion **16**, 546 (1976).

[13]P. H. Rebut and B. J. Green, in *Plasma Physics and Controlled Nuclear Fusion Research 1976,* Proceedings of the 6th International Conference, Berchtesgaden (IAEA, Vienna, 1977), Vol. 2, p. 3.

[14]N. Ohyabu, Nucl. Fusion **19**, 1491 (1979).

[15]D. E. T. F. Ashby and M. H. Hughes, Nucl. Fusion **21**, 91 (1981).

[16]D. E. Roberts, Nucl. Fusion **23**, 311 (1983).

[17]F. W. Perkins and R. A. Hulse, Phys. Fluids **28**, 1837 (1985).

[18]D. E. Post, R. V. Jensen, C. B. Tarter, W. H. Grassberger, and W. A. Lokke, At. Data Nucl. Data Tables **20**, 397 (1977).

[19]K. Behringer, A. Boileau, F. Bombarda, G. B. Denne, W. Engelhardt, M. J. Forrest, G. Fussmann, R. Giannella, N. A. Gottardi, M. Von Hellermann, L. Horton, H. Jäckel, C. Jupén, E. Källne, K. D. Lawson, G. Magyar, G. M. McCracken, P. D. Morgan, E. R. Müller, N. J. Peacock, J. Ramette, B. Saoutic, M. F. Stamp, H. P. Summers, G. Tallents, and A. Weller, in *Plasma Physics and Controlled Nuclear Fusion Research 1986,* Proceedings of the 11th International Conference, Kyoto (IAEA, Vienna, 1987), Vol. 1, p. 197.

[20]D. J. Campbell, P. A. Duperrex, A. W. Edwards, R. D. Gill, C. W. Gowers, R. S. Granetz, M. Hugon, N. Lopes Cardozo, M. Malacarne, D. C. Robinson, F. C. Schüller, P. Smeulders, J. A. Snipes, P. E. Stott, G. Tonetti, B. J. D. Tubbing, A. Weller, and J. A. Wesson, in *Plasma Physics and*

Controlled Nuclear Fusion Research 1986, Proceedings of the 11th International Conference, Kyoto (IAEA, Vienna, 1987), Vol. 1, p. 433.

[21] R. A. Hulse, Nucl. Technol./Fusion **3**, 259 (1983).

[22] Glenn Bateman, Bull. Am. Phys. Soc. **32**, 1917 (1987).

[23] R. J. Hawryluk, V. Arunasalam, J. D. Bell, M. G. Bell, M. Bitter, et al., Princeton Plasma Physics Laboratory Report No. PPPL-2390 (1986).

[24] INTOR Group, *International Tokamak Reactor, Phase Two A, Part II*, Report of the International Tokamak Reactor Workshop, 1984 & 1985, (IAEA, Vienna, 1986).

[25] M. Greenwald, D. Gwinn, S. Milora, J. Parker, R. Parker, S. Wolfe, M. Besen, B. Blackwell, F. Camacho, S. Fairfax, C. Fiore, M. Foord, R. Gandy, C. Gomez, R. Granetz, B. LaBombard, B. Lipschultz, B. Lloyd, E. Marmar, S. McCool, D. Pappas, R. Petrasso, M. Porkolab, P. Pribyl, J. Rice, D. Schuresko, Y. Takase, J. Terry, and R. Watterson, in *Plasma Physics and Controlled Nuclear Fusion Research 1984*, Proceedings of the 10th International Conference, London (IAEA, Vienna, 1985), Vol. 1, p. 45.

[26] C. S. Chang and F. L. Hinton, Phys. Fluids **25**, 1493 (1982).

[27] M. H. Redi, W. M. Tang, P. C. Efthimion, D. R. Mikkelsen, and G. L. Schmidt, Nucl. Fusion **27**, 2001 (1988).

[28] C. B. Tarter, J. Spectros. Radia. Trans. **10**, 531 (1977).

[29] G. Bateman, Princeton Plasma Physics Laboratory Report No. PPPL-2373 (1986); Fusion Technol. (in press).

[30] B. B. Kadomtsev, Sov. J. Plasma Phys. **1**, 389 (1975). B **13**, 3895 (1980).

[31] D. P. Stotler and Glenn Bateman, in *Proceedings of the Sherwood Theory Meeting, Gatlinburg, Tennessee, 1988* (Oak Ridge National Laboratory, Oak Ridge, 1988), Paper 3D37.

[32] J. D. Strachan, F. P. Boody, C. Bush, B. Grek, R. J. Hawryluk, D. Heifetz, H. W. Hendel, K. W. Hill, D. W. Johnson, A. T. Ramsey, S. Sesnic, J. F. Schivell, M. Shimada, G. Taylor, and M. C. Zarnstorff, in *Proceedings of the European Conf. on Plasma Physics and Controlled Fusion* (European Physical Society, Budapest, Hungary, 1985), Part I, p. 339.

[33] J. D. Strachan, F. P. Boody, C. E. Bush, S. A. Cohen, B. Grek, L. Grisham, F. C. Jobes, D. W. Johnson, D. K. Mansfield, S. S. Medley, W. Morris, H. K. Park, J. Schivell, G. Taylor, K. L. Wong, S. Yoshikawa, M. C. Zarnstorff, and S. J. Zweben, J. Nucl. Mater. **145 - 147**, 186 (1987).

[34] John Wesson, *Tokamaks* (Clarendon Press, New York, 1987).

[35] A. Sykes and J. A. Wesson, Phys. Rev. Lett. **44**, 18 (1980).

[36] D. Bartlett, D. Campbell, A. Costley, P. A. Duperrex, A. Edwards, R. Gill, N. Gottardi, R. Granetz, P. Haynes, T. Hender, M. Hugon, H. Jäckel, E. Lazzaro, N. Lopes Cardozo, M. Lorentz Gottardi, T. Oyevaar, N. Salmon, F. Schüller, P. Smeulders, J. Snipes, P. Stott, G. Tonetti, D. Ward, A. Weller, and J. Wesson, Bull. Am. Phys. Soc. **32**, 1838 (1987).

[37] C. Z. Cheng, H. P. Furth, and A. H. Boozer, Plasma Phys. and Controlled Fusion **29**, 351 (1987).

[38] S. P. Hirshman and D. J. Sigmar, Nucl. Fusion **21**, 1079 (1981).

[39] F. Alladio and G. Vlad, Phys. Fluids **31**, 602 (1988).

[40] R. A. Hulse, D. E. Post, and D. R. Mikkelsen, J. Phys. B **13**, 3895 (1980).

[41] J. M. Ogden, C. E. Singer, D. E. Post, R. V. Jensen, and F. G. P. Seidl, IEEE Trans. Plasma Sci. **PS-9**, 274 (1981).

run	Z	scan	profile	q_{cyl}	$\overline{n}_{e,19}$	I_p	B_T	$\overline{n}_{e,19}R/B_T$
02d	22	I_p, B_T	peaked	2.8	4.70	1.50	3.20	3.77
02f	22	I_p, B_T	peaked	3.4	4.70	1.42	3.71	3.26
02g	22	I_p, B_T	peaked	3.9	4.70	1.41	4.22	2.86
02h	22	I_p, B_T	peaked	4.4	4.70	1.29	4.38	2.76
02i	22	I_p, B_T	flat	2.8	4.70	1.13	2.41	5.01
02j	22	I_p, B_T	flat	3.4	4.70	0.82	2.48	4.87
02k	22	I_p, B_T	flat	3.9	4.70	0.92	2.40	5.03
02l	22	I_p, B_T	flat	4.4	4.70	0.78	2.62	4.61
03c	22	$\overline{n}_e$	peaked	2.8	6.30	2.20	4.70	3.44
03d	22	$\overline{n}_e$	peaked	3.9	6.60	2.20	6.60	2.57
05b	6	$\overline{n}_e$	peaked	2.8	10.0	2.20	4.70	5.47
05c	6	$\overline{n}_e$	peaked	3.9	9.90	2.20	6.60	3.86
06a	6	I_p, B_T	peaked	2.8	8.00	1.70	3.63	5.66
06b	6	I_p, B_T	peaked	3.9	8.00	1.66	4.99	4.12
06c	6	I_p, B_T	flat	2.8	6.00	1.75	3.74	4.12
06e	6	I_p, B_T	flat	3.9	6.00	1.47	4.40	3.50

Table I: Simulation parameters; Z indicates impurity atomic number. Flat and peaked describe the density profile. Units are $\overline{n}_{e,19}$: 10^{19} m^{-3}. B_T : T. I_p : MA, and $R = 2.57$ m.

run	$\overline{n}_{e,19}/(B_T^{0.09}I_p^{0.59})$	$\overline{n}_{e,19}/I_p$
02d	3.33	3.13
02f	3.41	3.31
02g	3.38	3.33
02h	3.53	3.64
03c	3.43	2.86
03d	3.51	3.30

Table II: Constant required in Eq. (36) and in $\overline{n}_e \propto I_p$ by data in Table I.

run	$\overline{n_e}_{,19}/(B_T^{0.84}I_p^{-0.16})$	$\overline{n_e}_{,19}/B_T$
02i	2.29	1.95
02j	2.13	1.90
02k	2.23	1.96
02l	2.01	1.79

Table III: Constant required in Eq. (36) and in $\overline{n_e} \propto B_T$ by data in Table I.

Figures

FIG. 1. Dependence of the radiated power per unit volume. divided by the impurity and electron densities on electron temperature. for (a) titanium and (b) carbon computed from results of Refs. 18 and 28. respectively.

FIG. 2. Dependence of the average charge in coronal equilibrium on electron temperature for (a) titanium and (b) carbon computed from results of Refs. 18 and 28, respectively.

FIG. 3. Plot of the data from Table I in Hugill space. Lines for $\overline{n_e} = B_T/Rq_{cyl}$ and $\overline{n_e} = 2B_T/Rq_{cyl}$ are included for comparison. In (a) and (b) we show data from runs with titanium impurity; in (c), carbon was used. Open (closed) markers indicate peaked (flat) density profiles. Also I_p, B_T scans are denoted by square markers, and $\overline{n_e}$ scans by circular markers.

FIG. 4. Electron temperature as a function of time and radial half-width for simulation 02h.

FIG. 5. Toroidal current density as a function of simulation time and radial half-width for run 03d.

FIG. 6. Electron density as a function of radial half-width for 02h and 02l. In both cases. the profiles were taken at the end of the initial (uncontracted) steady state.

FIG. 7. Electron density as a function of radial half-width and time for simulation 06e.

FIG. 8. Radiated power per unit volume given by Eq. (9) as a function of time and radial half-width for simulation 02h.

FIG. 9. Radiated power per unit volume given by Eq. (9) as a function of time and radial half-width for simulation 02j.
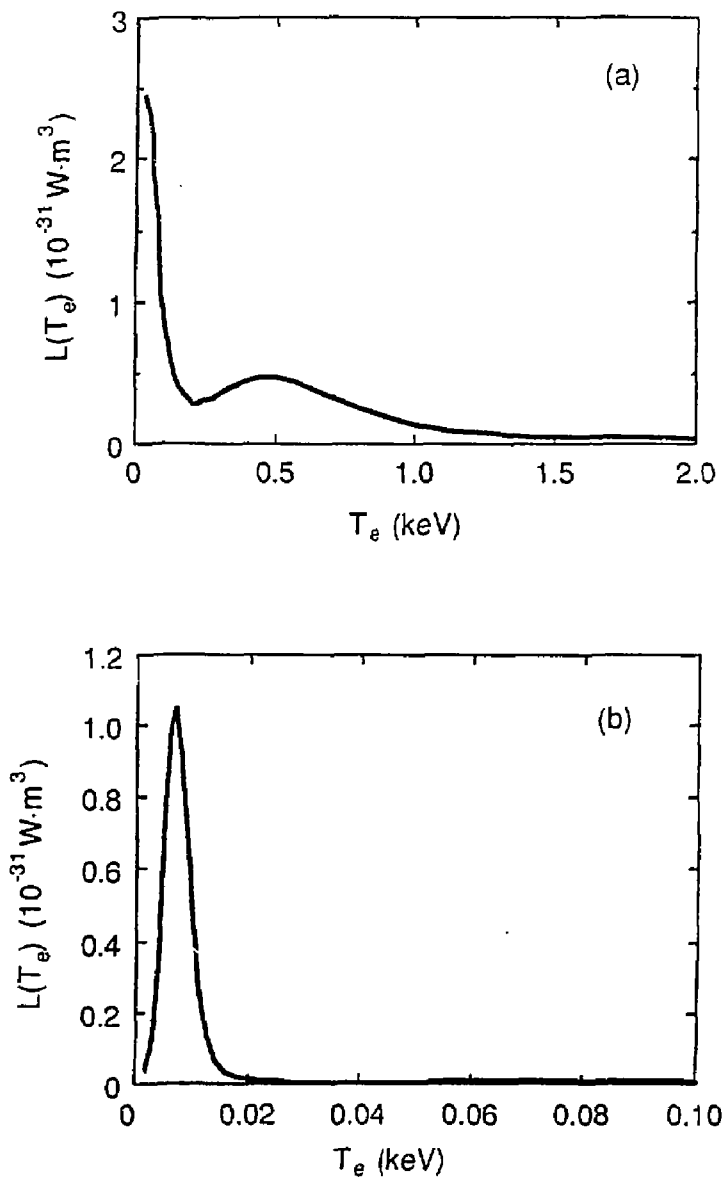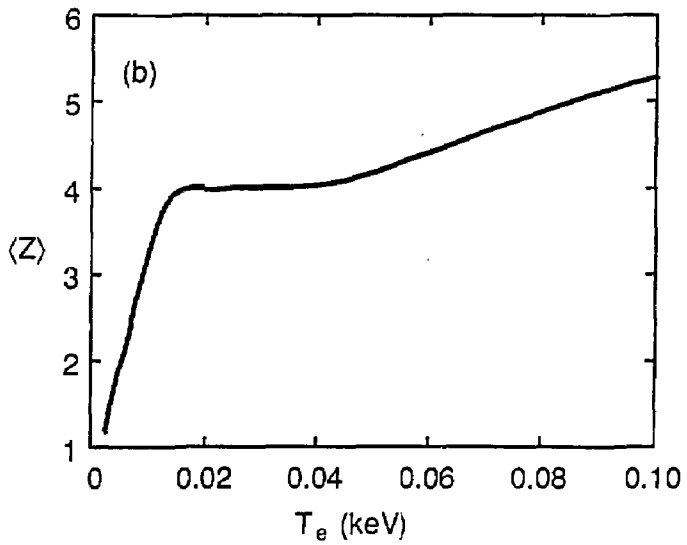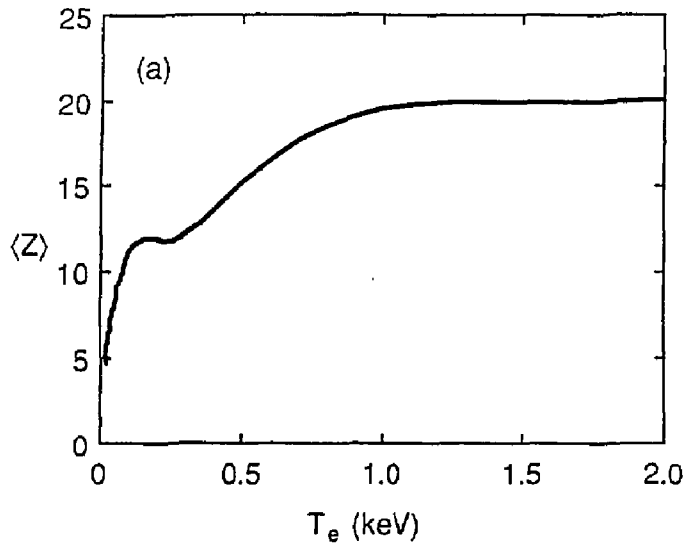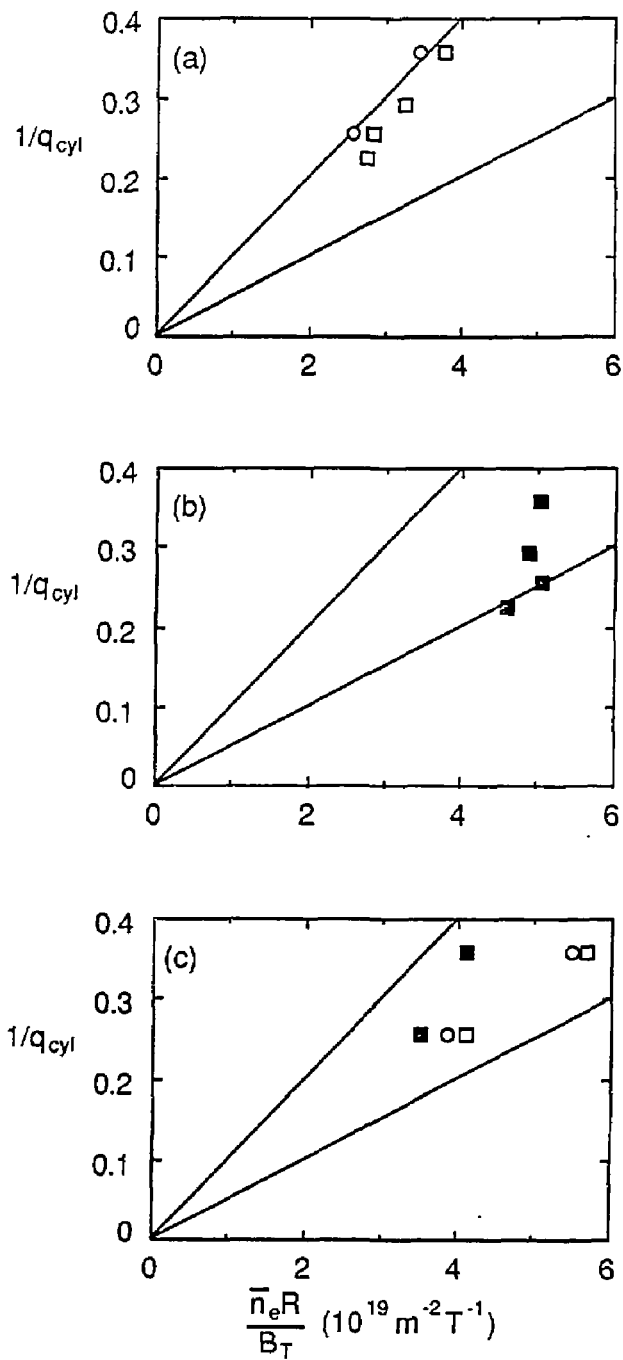
FIG. 1

FIG. 2

FIG. 3
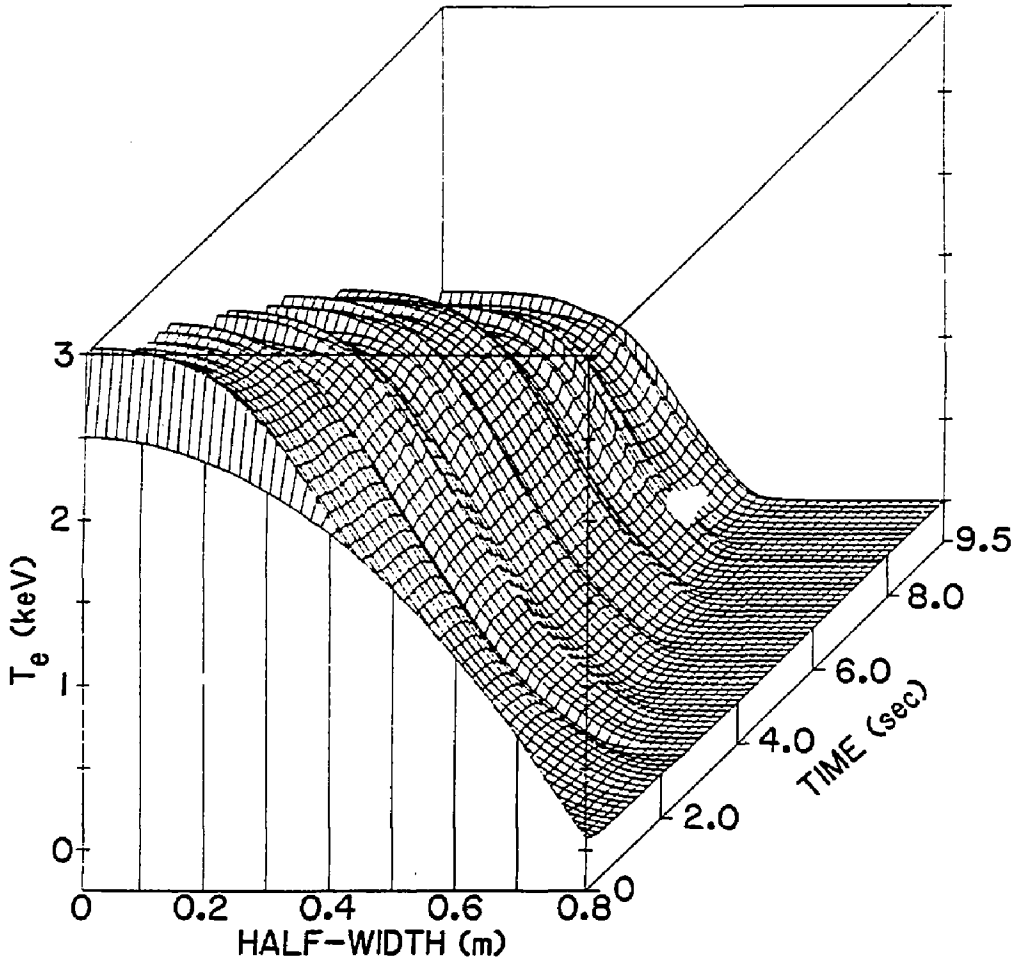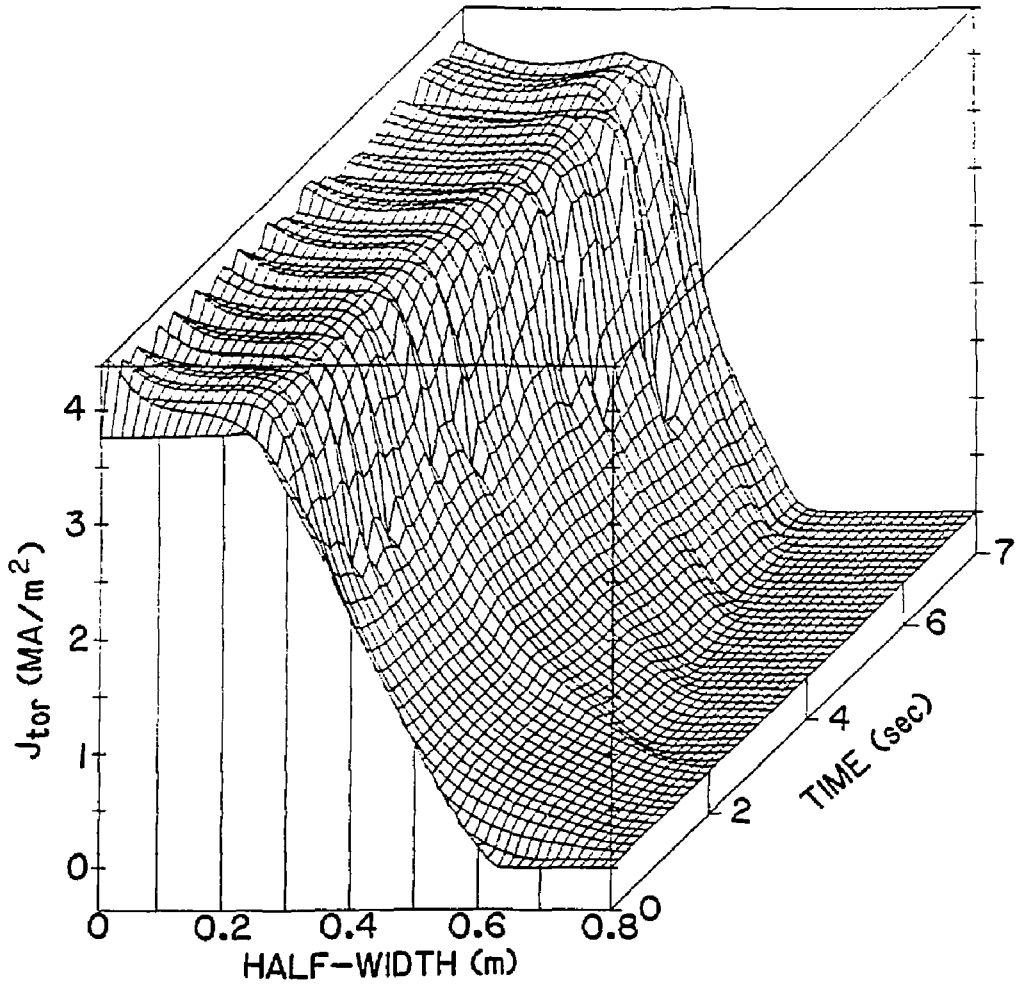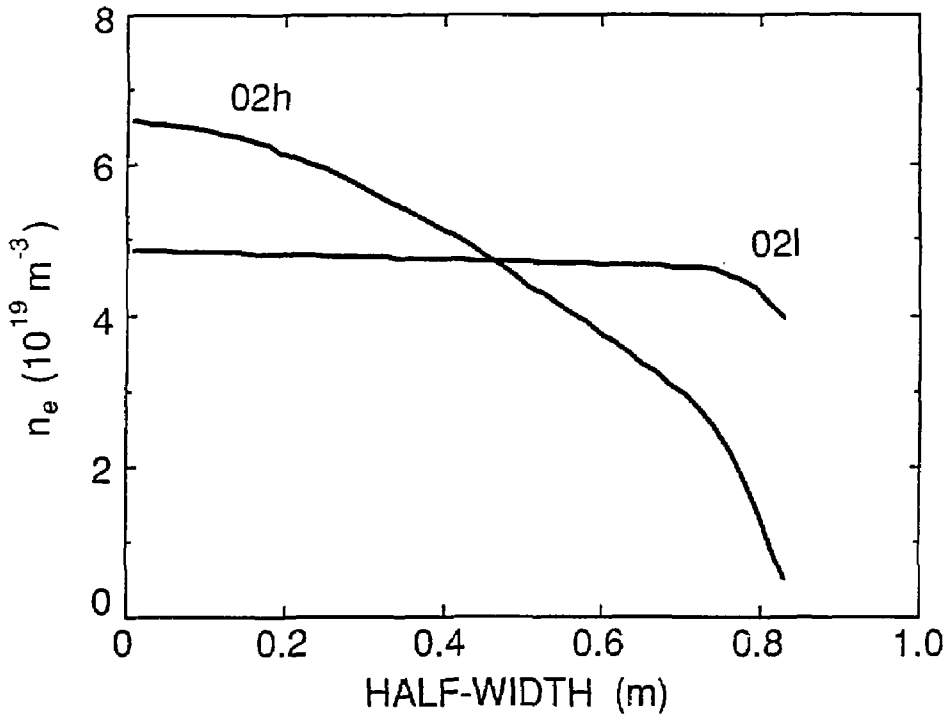
37

#88P0073

FIG. 4

38

#88P0072

FIG. 5

FIG. 6

#88P0070

n_e ($10^{19} m^{-3}$)

HALF-WIDTH (m)

TIME (sec)

FIG. 7

41
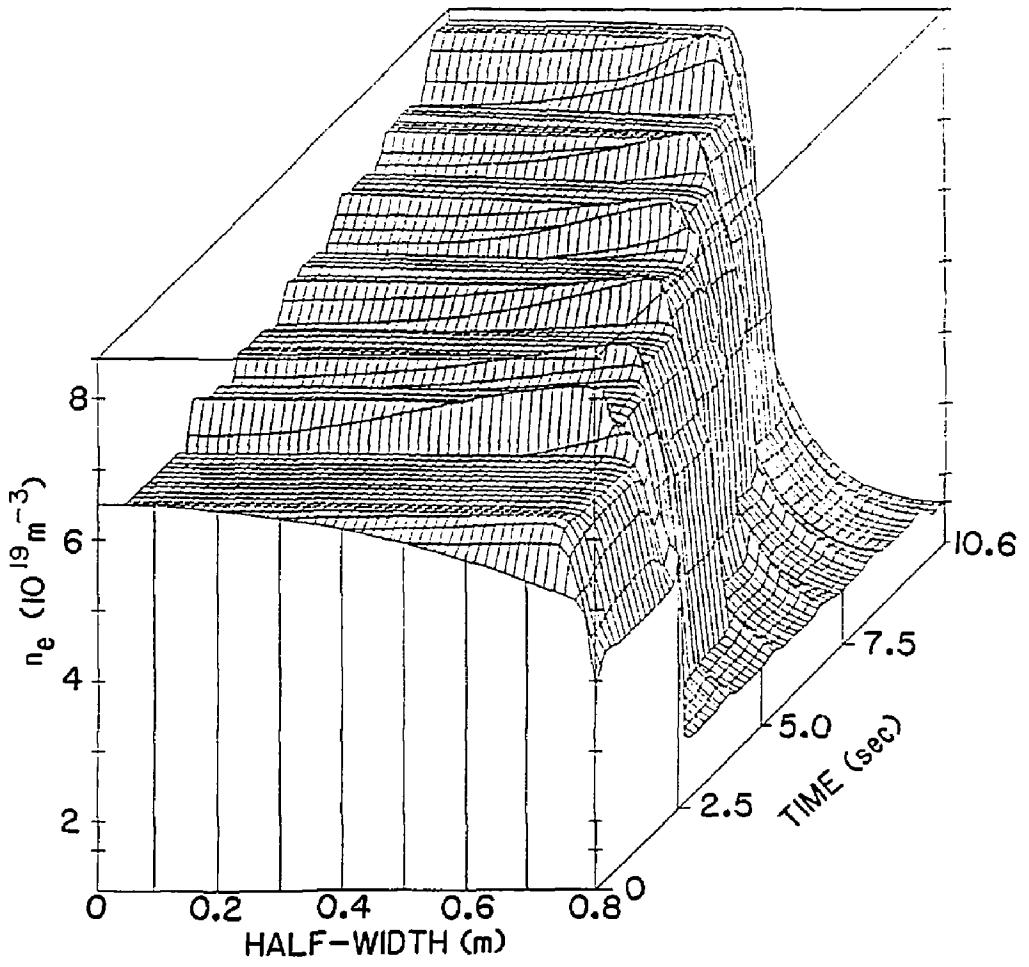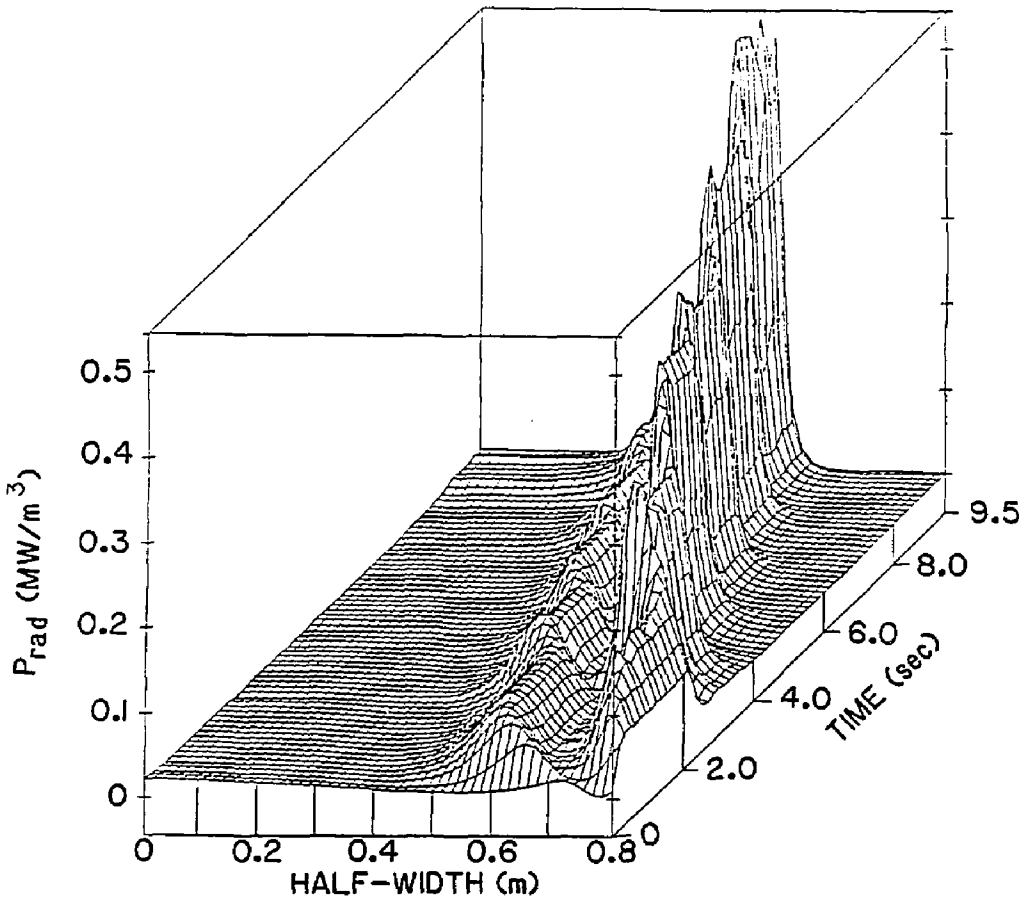
FIG. 8
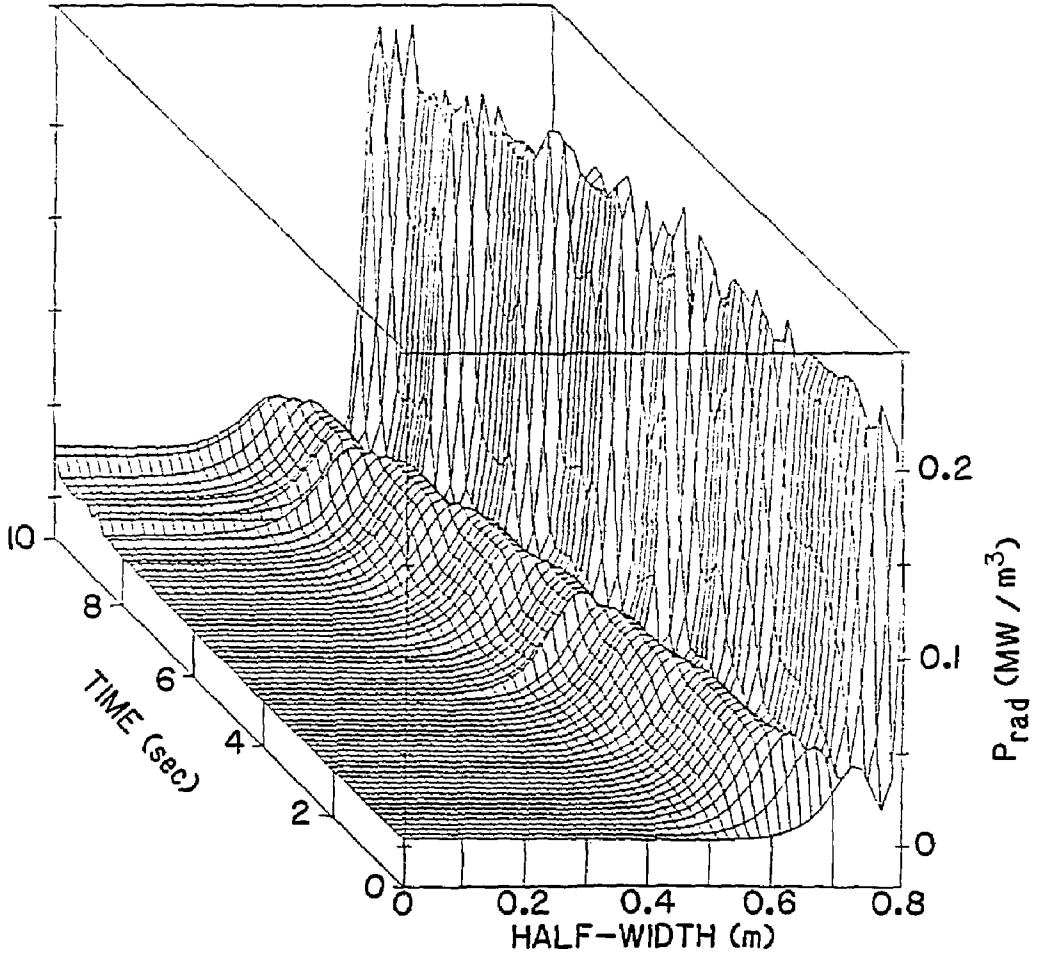
FIG. 9

Dr. Frank J. Paoloni, Univ of Wollongong, AUSTRALIA
Prof. M.H. Brennan, Univ Sydney, AUSTRALIA
Plasma Research Lab., Australian Nat. Univ., AUSTRALIA
Prof. I.R. Jones, Flinders Univ., AUSTRALIA
Prof. F. Cap, Inst Theo Phys, AUSTRIA
Prof. M. Heindler, Institut fur Theoretische Physik, AUSTRIA
M. Goossens, Astronomisch Instituut, BELGIUM
Ecole Royale Militaire, Lab de Phys Plasmas, BELGIUM
Commission-European, Dg-XII Fusion Prog, BELGIUM
Prof. R. Boucique, Laboratorium voor Natuurkunde, BELGIUM
Dr. P.H. Sakanaka, Instituto Fisica, BRAZIL
Instituto De Pesquisas Espaciasi-INPE, BRAZIL
Documents Office, Atomic Energy of Canada Limited, CANADA
Dr. M.P. Bachynski, MPB Technologies, Inc., CANADA
Dr. H.M. Skarsgard, University of Saskatchewan, CANADA
Dr. H. Barnard, University of British Columbia, CANADA
Prof. J. Teichmann, Univ. of Montreal, CANADA
Prof. S.R. Sreenivasan, University of Calgary, CANADA
Prof. Tudor W. Johnston, INRS-Energie, CANADA
Dr. C.R. James, Univ. of Alberta, CANADA
Dr. Peter Lukac, Komenskeho Univ, CZECHOSLOVAKIA
The Librarian, Culham Laboratory, ENGLAND
The Librarian, Rutherford Appleton Laboratory, ENGLAND
Mrs. S.A. Hutchinson, JET Library, ENGLAND
C. Mouttet, Lab. de Physique des Milieux Ionises, FRANCE
J. Radet, CEN/CADARACHE - Bat 506, FRANCE
Univ. of Ioannina, Library of Physics Dept. GREECE
Dr. Tom Musl, Academy Bibliographic Ser., HONG KONG
Preprint Library, Hungarian Academy of Sciences, HUNGARY
Dr. B. Dasgupta, Saha Inst of Nucl. Phys., INDIA
Dr. P. Kaw, Institute for Plasma Research, INDIA
Dr. Philip Rosenau, Israel Inst. Tech, ISRAEL
Librarian, Int'l Ctr Theo Phys, ITALY
Prof. G. Rostagni, Univ Di Padova, ITALY
Miss Clelia De Palo, Assoc EURATOM-ENEA, ITALY
Biblioteca, Instituto di Fisica del Plasma, ITALY
Dr. H. Yamato, Toshiba Res & Dev, JAPAN
Prof. I. Kawakami, Atomic Energy Res. Institute, JAPAN
Prof. Kyoji Nishikawa, Univ of Hiroshima, JAPAN
Direc. Dept. Large Tokamak Res. JAERI, JAPAN
Prof. Satoshi Itoh, Kyushu University, JAPAN
Research Info Center, Nagoya University, JAPAN
Prof. S. Tanaka, Kyoto University, JAPAN
Library, Kyoto University, JAPAN
Prof. Nobuyuki Inoue, University of Tokyo, JAPAN
S. Mori, JAERI, JAPAN
Librarian, Korea Advanced Energy Res. Institute, KOREA
Prof. D.I. Choi, Adv. Inst Sci & Tech, KOREA
Prof. B.S. Liley, University of Waikato, NEW ZEALAND
Institute of Plasma Physics, PEOPLE'S REPUBLIC OF CHINA
Librarian, Institute of Phys., PEOPLE'S REPUBLIC OF CHINA
Library, Tsing Hua University, PEOPLE'S REPUBLIC OF CHINA

Z. Li, Southwest Inst. Physics, PEOPLE'S REPUBLIC OF CHINA
Prof. J.A.C. Cabral, Inst Superior Tecnico, PORTUGAL
Dr. Octavian Petrus, AL I CUZA University, ROMANIA
Dr. Johan de Villiers, Fusion Studies, AEC, SO AFRICA
Prof. M.A. Hellberg, University of Natal, SO AFRICA
C.I.E.M.A.T., Fusion Div. Library, SPAIN
Dr. Lennart Stenflo, University of UMEA, SWEDEN
Library, Royal Inst Tech, SWEDEN
Prof. Hans Wilhelmson, Chalmers Univ Tech, SWEDEN
Centre Phys des Plasmas, Ecole Polytech Fed, SWITZERLAND
Bibliotheek, Fom-Inst Voor Plasma-Fysica, THE NETHERLANDS
Dr. D.D. Ryutov, Siberian Acad Sci, USSR
Dr. G.A. Eliseev, Kurchatov Institute, USSR
Dr. V.A. Glukhikh, Inst Electrophysical Apparatus, USSR
Dr. V.T. Tolok, Inst. Phys. Tech. USSR
Dr. L.M. Kovrizhnykh, Institute Gen. Physics, USSR
Nuclear Res. Establishment, Julich Ltd., W. GERMANY
Bibliothek, Inst. Fur Plasmaforschung, W. GERMANY
Dr. K. Schindler, Ruhr Universitat Bochum, W. GERMANY
ASDEX Reading Rm, IPP/Max-Planck-Institut fur
   Plasmaphysik, W. GERMANY
Librarian, Max-Planck Institut, W. GERMANY
Prof. R.K. Janev, Inst Phys, YUGOSLAVIA